ADVANCED OPTICAL MATERIALS
www.advopticalmat.de

Check for updates

The Impact of Grain Boundaries on Charge Transport in Polycrystalline Organic Field-Effect Transistors

*Tobias Meier, Heinz Bässler, and Anna Köhler**

Dedicated to Professor Karl Leo on the occasion of his 60th birthday

The active element of an organic field effect transistor (OFET) is a polycrystalline transport layer. The crystallites are interrupted by grain boundaries (GB) that can act as traps or barriers to the charge-carriers. Their impact on charge transport and hence on the performance of the OFET is still not fully understood. Employing kinetic Monte Carlo studies, the authors set up well-defined test systems and explore how the parameters of the system, for example, the thickness of the GB, their fractional contribution to the overall film, and the energies of the GB relative to the crystallites, affect the performance of the OFET. It is found that these parameters control the position of the Fermi level, which is crucial in controlling whether the charge transport is confined to GB, or whether it takes place as a superposition between filamentary transport in the boundaries and delocalized transport in the crystallites, or as tunneling-mediated transport across the crystallites. Guidelines for the morphological optimization of the films for these different transport modes are derived.

1. Introduction

Organic semiconductors have seen a development that can be considered as exponential. It was initiated by the discovery that a molecular crystal can emit light upon application of an electric field.[1] Early on it was recognized that this effect is caused by the recombination of electrons and holes from appropriate electrodes. However, it was a long way to commercialize this idea and finally to fabricate TV screens of unprecedented brilliance. One of the pioneers in this development is Karl Leo. He recognized that exploiting the phenomenon of electroluminescence requires interaction between optics and electronics, because emission from an organic light emitting diode (OLED) is controlled by the electric circuit. For large display panels an active matrix is required, where transistors address the individual pixels. While those used in commercial active matrix displays are often made from amorphous silicon, organic field effect transistors (OFETs) offer several competitive advantages. They allow for low temperature and low cost processing, and their excellent mechanical flexibility can help to fully exploit the potential of OLEDs, for example, for large area applications and truly flexible substrates.[2]

OFETs have technically evolved since their first reports more than 30 years ago,[3] with charge-carrier mobility values now reaching more than 1–10 cm^2 V^{-1} s^{-1}.[4] This progress has only been possible through advancements in both, in our theoretical understanding on how charge transport in OFETs works,[5] as well as in the progress with experimental techniques such as synthesis,[6] film processing,[7] and device engineering.[2,8] From a theoretical perspective, it is clear that the packing of the individual molecules or polymer segments in the film determines the overlap of wavefunctions between adjacent sites, and thus the transfer integrals. These transfer integrals, which can be on the order of up to 100 meV, become modulated through the effect of low frequency intermolecular vibrations that cause transient localization of the carrier wavefunction at room temperature, thus intrinsically limiting the observed mobility.[5e] Further, extrinsic limitations come through surface and bulk traps as well as through grain boundaries (GB) between crystallites. In principle, such extrinsic effects can be controlled through careful film processing, yet one needs to balance the effort spent with the improvement on mobility that can be obtained. Thus, there is a need for a detailed understanding on the influence of defects on charge transport. While surface and bulk traps have received much experimental attention,[9] there is still a need for more theoretical and simulation studies on the role of GB[10,11] in particular since their critical role in controlling mobility is experimentally well documented.[12] An exception are semicrystalline polymer films where the important role of tie chains in ensuring high inter-grain transfer rates has been identified as a major factor contributing to high overall mobilities, alongside with small angles between adjacent grains.[13]

In this work, we use kinetic Monte Carlo (kMC) simulations of charge transport in an OFET to assess the impact of GB on

T. Meier, Prof. A. Köhler
Soft Matter Optoelectronics and Bavarian Polymer Institute (BPI)
University of Bayreuth
Universitätsstraße 30, 95440 Bayreuth, Germany
E-mail: anna.koehler@uni-bayreuth.de
Prof. H. Bässler, Prof. A. Köhler
Bayreuth Institute of Macromolecular Research (BIMF)
University of Bayreuth
Universitätsstraße 30, 95440 Bayreuth, Germany

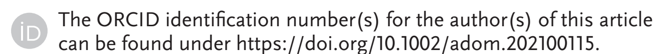
The ORCID identification number(s) for the author(s) of this article can be found under https://doi.org/10.1002/adom.202100115.

© 2021 The Authors. Advanced Optical Materials published by Wiley-VCH GmbH. This is an open access article under the terms of the Creative Commons Attribution License, which permits use, distribution and reproduction in any medium, provided the original work is properly cited.

DOI: 10.1002/adom.202100115

 © 2021 The Authors. Advanced Optical Materials published by Wiley-VCH GmbH

the overall charge-carrier mobility and their activation energy. kMC simulations have proven to be a successful tool to study the transport of charges.[14] For example, Bobbert et al. have employed kMC simulations to establish that charge transport in OFETs cannot be considered as a mere 2D process and confined to one or two in-plane layers, even though the charge density is confined to the first one or two monolayers. Rather, hopping in direction perpendicular to the semiconductor layer is an essential part of charge transport, even for high gate biases.[15] Similarly, Brédas and coworkers used kMC simulations to address the microscopic nature of charge transport and the validity of the gradual channel approximation.[16] The impact of mismatches in crystallite orientations on charge transport has been addressed by combining molecular dynamics calculations with kMC simulations in the groups of Andrienko and Nelson.[10a]

In general, GB in polycrystalline morphologies are well known to be detrimental to charge transport.[12a,d,17] They can act as traps or barriers for charge-carriers, depending on the position of the mean energy in the GB relative to that of the crystalline domains, and there is experimental evidence for both.[9,10,18] Traps have been identified in different organic semiconductors through Kelvin probe force microscopy,[19] time-resolved electric force microscopy,[20] from comparing the hole trap density of states (DOS),[17a] as well as from electronic structure calculations.[21] GB that are barriers for charge-carriers have been recognized through conducting probe atomic force microscopy.[22] It is further argued that though GB are traps to charge-carriers they can act as barriers when the traps are filled due to their repulsive electrostatic potential.[17d,23] The role of GB as barriers is supported further through electronic structure calculations[24] as well as energy landscape calculations from molecular dynamics.[10a]

Here, we consider both, energetic traps and barriers. We investigate how the physical width of the GB, the energetic depth or height, as well as the grain size and thus the resulting fraction of crystalline phase impacts on charge transport in polycrystalline OFETs. The answers to these questions will help to derive strategies regarding which materials to use and how to process them. For our kMC approach, we use a simple algorithm to create polycrystalline morphologies on a grid lattice that are taken representative for molecular films. From the charge-carrier mobility and its temperature dependence we draw conclusions about the impediments caused by different types of GB on the nature of charge transport in such polycrystalline systems.

2. Computational Method

We simulated charge transport in an OFET with the commercially available software Bumblebee (Simbeyond B.V., simbeyond.com) through kinetic Monte–Carlo simulation. Charge transport is simulated as a thermally activated hopping process using Miller–Abrahams hopping rates asshown in Equation (1):[25]

$$k_{ij} = \nu_0 \exp\left(-2\gamma |r_{ij}|\right) \begin{cases} \exp\left(-\dfrac{\Delta E_{ij}}{kT}\right) & \Delta E_{ij} > 0 \\ 1 & \Delta E_{ij} \leq 0 \end{cases} \tag{1}$$

where ν_0 is the attempt-to hop frequency, γ the inverse localization length, and r_{ij} the distance between sites i and j. We chose $\nu_0 = 10^{13}$ s^{-1} for jumps between crystallites as well as to, from and within GB, we used $\nu_0 = 10^{15}$ s^{-1} for jumps within crystallites, and we always used $\gamma = 5$ nm^{-1}. We considered jumps up to the second nearest neighbor in every direction. ΔE_{ij} is the energy difference between sites i and j, k_B the Boltzmann constant and T the temperature. The site energies include the energetic disorder of the semiconductor within the Gaussian disorder model,[26] the drop of the electrostatic potential of the gate electrode over the film (z direction), the applied electric field in source–drain direction (x direction) and the Coulomb interaction between all charge-carriers. Up to a mutual distance of 10 nm, the Coulomb interaction between the carriers is calculated explicitly. Beyond this cut-off radius, a mean value is used.[27]

Charge transport in the OFET is modeled as shown in **Figure 1**. We consider a semiconductor layer between the source and drain electrode. An electric field of $F = 6 \times 10^4$ V cm^{-1}, typical for OFET operation, is acting along source–drain direction. We note that charge-carrier injection and extraction, and thus any effects due to contact resistance, are not explicitly simulated. Rather, periodic boundary conditions are applied to the semiconductor layer in the x and y direction. The semiconductor is separated from the gate electrode by a dielectric of 100 nm thickness. The dielectric constant is set to 4, which is a good value for organic semiconductors and approximately the value of SiO_2 as a material for the gate dielectric.[28] Image charges due to the metallic electrodes are considered as well but do not play a significant role due to the large thickness of the dielectric ($d_{\text{dielectric}}$ = 100 nm). The voltage at the gate electrode is 5 V corresponding to a gate electric field of $F = 5 \times 10^5$ V cm$^{-1,}$ so that the transistor is in the linear regime. To implement the gate electric field and to create the channel in the simulation, the software Bumblebee treats the vertical structure like a capacitor and proceeds by the following steps. First, the potential at the gate electrode is set to 5 V with respect to a fictitious reference electrode on top of the semiconductor where the potential is set to 0 V. This creates an initially homogeneous electric field along z-direction. In a second step, a number of carriers are added randomly to the semiconductor according to the charge density expected, $\rho = \frac{\varepsilon_0 \varepsilon_r}{d} V$, where d is the thickness of the dielectric. Next, Bumblebee calculates

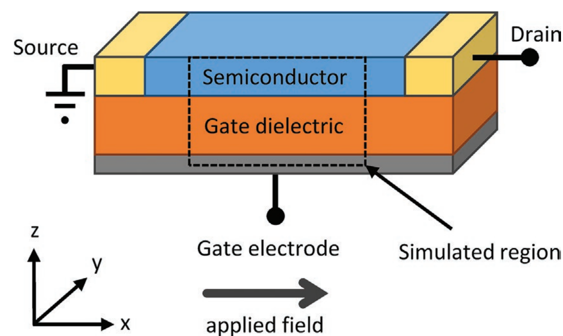

Figure 1. Geometry of the simulated OFET. Only the charge transport in the semiconductor layer is simulated, injection and extraction are replaced by periodic boundary conditions.

© 2021 The Authors. Advanced Optical Materials published by Wiley-VCH GmbH

how the charges move and accumulate at semiconductor/dielectric interface, as well as the screening effects on the field resulting from this charge carrier distribution. This is achieved by computing all the (time-dependent) Coulomb contributions to the field from all the carriers and their interactions. A final refinement of the gate field is obtained by accounting for the finite size effects of placing a finite integer number of charges in the simulation box. For this, the gate voltage is slightly adjusted until the mobile carriers in the OFET channel completely screen the field within the semiconductor. An applied gate voltage of 5 V implies a surface charge-carrier density of 0.011 charges per site if all charges were in the bottom-most in-plane layer. Slightly lower values apply for a (more realistic) modified vertical charge distribution. Any modification of the gate-induced surface charge-carrier density due to the potential drop from source to drain was not considered, that is, we work in the gradual channel approximation.

The morphology of the semiconductor layer is generated on a cubic grid with 1 nm lattice spacing. One semiconductor layer consists of 120×120 sites, with periodic boundary conditions in the x and y dimension (implying transport in an infinitely wide and long channel) and with 10 in-plane layers in z direction. The number of in-plane layers is sufficient since charge transport mostly takes places in the bottom-most in-plane layers, with few jumps to further in-plane layers.[15] The grid points represent localized sites of the organic semiconductor on which the charge-carriers move incoherently through hopping, that is, each grid point represents a molecule. Adjacent sites can be assigned to domains in order to mimic the polycrystalline morphology of the semiconductor. The domains are defined as crystallites of the semiconductor and the region between the crystallites represents the GB.

For the generation of the polycrystalline morphology an algorithm similar to that of Vladimirov et al. is used.[10b] In detail, crystallite growth is modelled by first defining seeds, equidistantly placed in the x-y plane, as sites from which the crystallites will start to grow in a 2D fashion. Each seed gets a random direction vector in the x-y plane representing the orientation of the crystallite with a monoclinic unit cell. The shape of the unit cell for every seed is the same. Next, the crystallites grow stepwise from the seeds. The crystallites grow up to a predefined width between the crystallites, henceforth designated as the GB width d_{GB}, and the growth stops when all possible sites are assigned. The resulting 2D structure is translated identically along the z-direction, implying a columnar-like structure with the GB as dividing walls. While a truly 3D crystallite growth would be required to model charge transport in 3D, the simplified approach used here is justified by the fact that transport is highly anisotropic and takes place in the lowest few in-plane layers, so that a true 3D crystal growth would lead to only minor differences. **Figure 2a**–d shows some snapshots during the crystallite growth process with Figure 2a corresponding to the initial seeds and Figure 2d to the final morphology. The underlying grid is not shown explicitly.

The sites of the crystallites have an energy from a Gaussian distribution centered ≈0 eV with a width of σ_{cryst} = 10 meV. We adopted this approach to account for a certain degree of dynamic disorder.[5e] The delocalization within the crystallites is taken into account through the 100 times higher prefactor for jumps within a crystallite than for jumps between different crystallites and within the GB. Due to this higher prefactor and the low energetic disorder, jumps within the crystallites are fast and more likely so that the behavior of a crystalline system is mimicked. The sites of the GB are assigned energies from a Gaussian distribution with a width of σ_{GB} = 50 meV around a center energy referred to as the GB energy E_{GB}. The higher disorder parameter represents the supposedly higher energetic disorder in the non-crystallite regions.[29] The center of the DOS of the GB is shifted with respect to the energetic center of the crystallite, as illustrated in Figure 2e.

We studied different morphologies that result from varying number of crystallite seeds N_{seeds} from 9 to 49 and 100 (initially set in arrays of 3×3, 7×7, or 10×10 seeds), the width of the GB d_{GB} from 1, 3 to 5 nm and the GB energy E_{GB} from −0.5 to

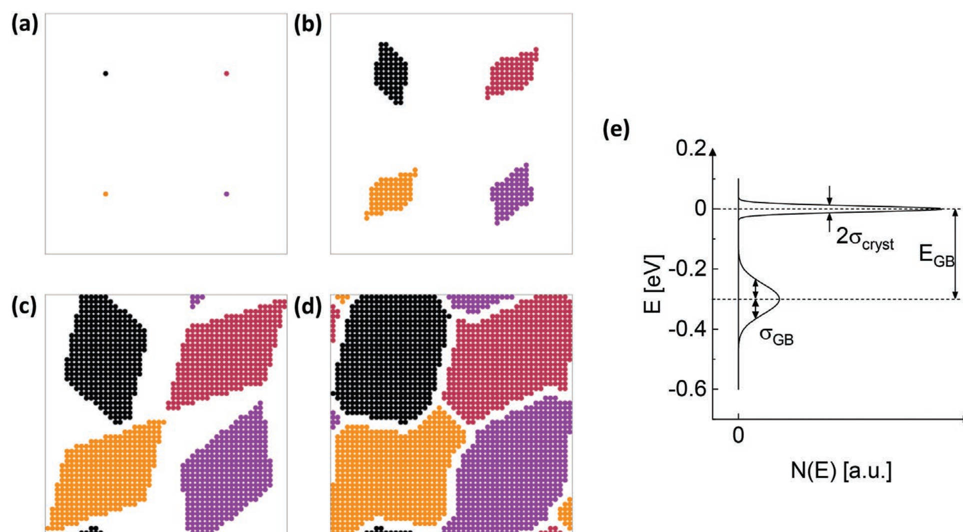

Figure 2. a–d) Snapshots of an exemplary polycrystalline morphology of the organic semiconductor layer during crystallite growth on a 2D grid. Image (a) shows the crystallite seeds and image (d) the final morphology. e) The distribution of site energies.

© 2021 The Authors. Advanced Optical Materials published by Wiley-VCH GmbH

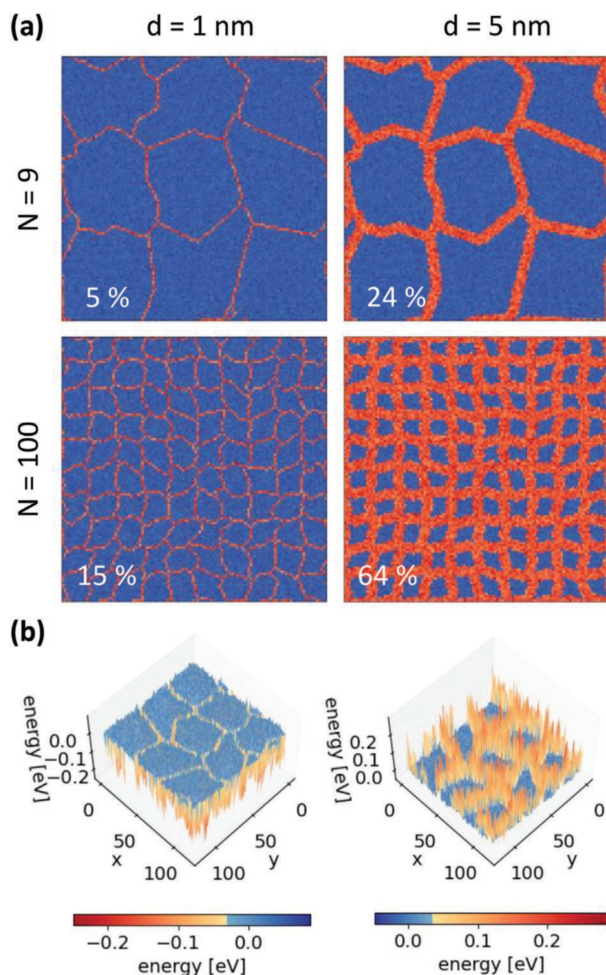

Figure 3. a) Four of the simulated morphologies of the polycrystalline semiconductor layer. Blue colors indicate the grains, the GB are drawn in orange colors. The number indicates the total volume taken up by the GB. b) Two polycrystalline energy landscapes as obtained from the morphology generation with traps (left) and barriers (right) as GB.

0.4 eV. With this, the mean diameter of the crystallites ranges from 5 (N_{seeds} = 100, d_{GB} = 5 nm) to 39 nm (N_{seeds} = 9, d_{GB} = 1 nm). Four of the simulated morphologies of the polycrystalline semiconductor are shown in **Figure 3**, along with two exemplary energy landscapes with traps and barriers as GB. The volume taken up by the GB ranges from 5%, when the crystallites are largest and the boundaries smallest, to 64% in the opposite case. The complete set of the simulated morphologies can be found in Figure S1, Supporting Information.

The simulation of the charge transport is performed until the current reaches steady state conditions or until a maximum simulation time, chosen to be 10^9 steps, is reached. The mean of the current density j in the device and its standard deviation are calculated from the latter part of the simulation close to the final attainment of equilibrium. From this, the charge-carrier mobility μ is calculated as in Equation (2):

$$\mu = \frac{j}{\varrho F} \tag{2}$$

where ϱ is the charge-carrier density and F the applied source-drain field. This approach does not consider any effects due to contact resistance at the electrodes.

3. Results

The calculated charge-carrier mobility for the different investigated morphologies as a function of the GB energy at room temperature (T = 300 K) is shown in **Figure 4**. All mobility values are given relative to that obtained for a single crystal with σ_{cryst} = 10 meV and apply to the case of a gate voltage set to 5 V. In the case that the centers of the DOS distributions for crystallites and GB are identical, that is, E_{GB} = 0, the mobility is maximal. Dependent on the width of the GB, the mobility drops by several orders of magnitude when the center energy of the GB is lower. The drop is stronger for thin GB than for large GB and depends on the number of crystallite seeds, which correlates with the

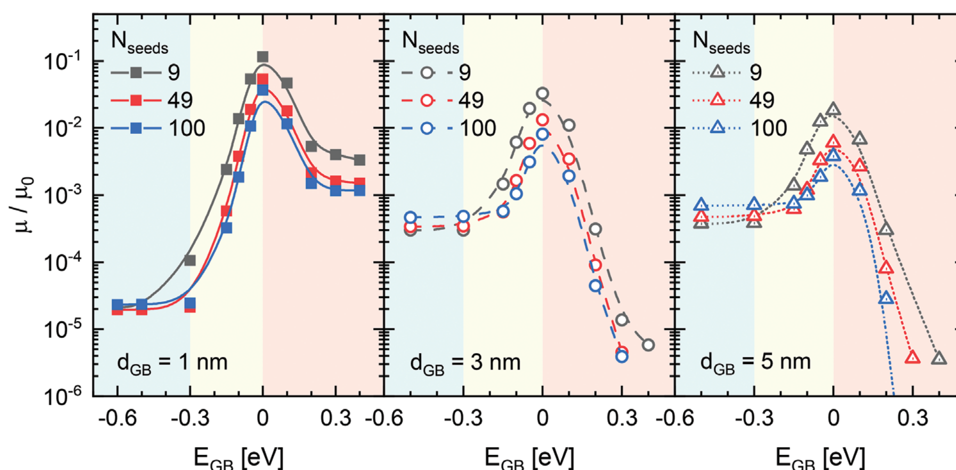

Figure 4. Calculated charge-carrier mobility from Monte–Carlo simulations as a function of the GB energy E_{GB} for different numbers of crystallite seeds as indicated. The width of the GB increases from left to right as indicated. The background color indicates the different charge transport regimes as explained in the text. The temperature is 300 K in all cases. The lines are guides to the eye.

© 2021 The Authors. Advanced Optical Materials published by Wiley-VCH GmbH

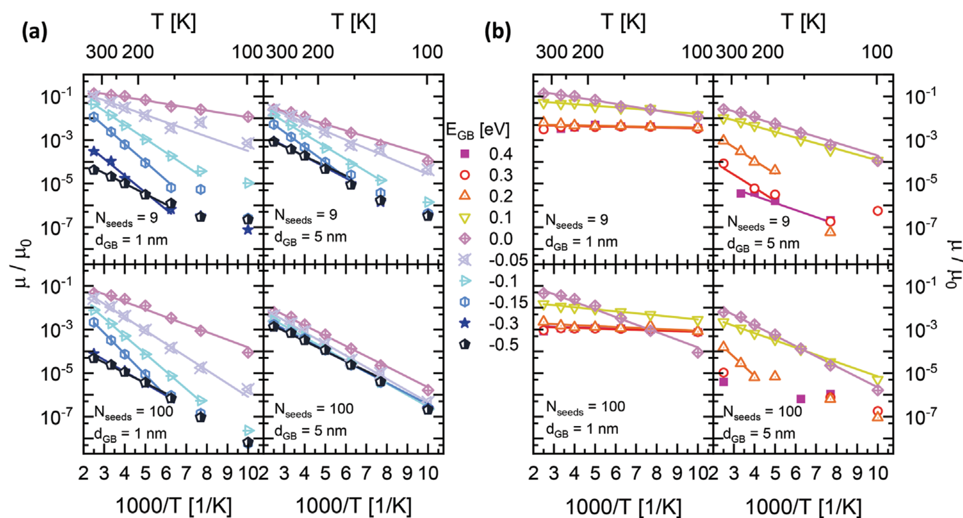

Figure 5. Temperature dependence of the charge-carrier mobility for different morphologies as indicated in the graphs. Lines are Arrhenius fits to the data in the range where the fit was applied. a) For -0.5 V $\leq E_{GB} \leq 0$, b) for $0 \leq E_{GB} \leq 0.4$ eV.

percentage of GB in the films. Fewer seeds imply larger crystallites so that the GB take up a lower fraction. The largest relative change of the mobility upon decreasing E_{GB} is observed for the thinnest GB and the lowest number of seeds, that is, the lowest fraction of GB. Below around $E_{GB} \leq -0.3$ eV, corresponding to $\approx 12\ k_BT$ at 300 K, the mobility is constant. In this regime, the mobility increases by a factor of ≈20 upon increasing the width of the GB from d_{GB} = 1 nm to 3 or 5 nm. Simultaneously, the mobility increases by a factor of 2 when the fraction of GB in the film increases. For $E_{GB} > -0.3$ eV, this trend is reversed, that is, the mobility is higher for larger crystallites with fewer GB, but the peak value decreases with increasing d_{GB}. When E_{GB} becomes positive, that is, the GB act as barriers for charge transport, the mobility decreases exponentially with increasing E_{GB} and becomes constant for d_{GB} = 1 nm. We will argue that this is a signature of tunneling through the GB. For $E_{GB} < 0.2$ eV the charge carriers can still surmount the barriers but for E_{GB} = 0.2 eV tunneling becomes the rate limiting process. This process is no longer possible when d_{GB} exceeds 1 nm. Note that the simulation algorithm involves a cut-off of the jump distance of 2 nm.

We calculated the mobility parametric in the GB energy for seven temperatures in the range from 100 to 400 K. This is presented in **Figure 5** as an Arrhenius-type plot and allows us to evaluate the temperature dependence of the mobility.

We first consider the transport when the GB represents traps. For the case of many seeds and large GB width, N_{seeds} = 100 and d_{GB} = 5 nm, transport is clearly Arrhenius-like with an activation energy that increases from 91 to 106 meV upon raising E_{GB} from −0.5 to −0.05 eV. In the other limiting case of N_{seeds} = 9 and d_{GB} = 1 nm, a similarly low activation energy of 95 meV is also observed for the deepest GB with E_{GB} = −0.5 eV, yet only down to a temperature of ≈150 K, from where the mobility remains constant. When the GB DOS is offset less with respect to the crystallite DOS, the observed high temperature activation energy is larger. It increases up to 164 meV at E_{GB} = −0.15 eV and then reduces again. The same trend is observed for the cases lying between these two limits, except for differences in the temperature above which the thermal activation applies. This evolution of the activation energy with E_{GB} is summarized in **Figure 6**. When the GB represent barriers (Figure 5b), we observe a weakly activated transport with 15 and 19 meV for E_{GB} = 0.1 eV and 9 or 100 seeds, respectively. For higher barriers, a temperature independent mobility results for the thinnest GB (d_{GB} = 1 nm), while transport gets impeded and

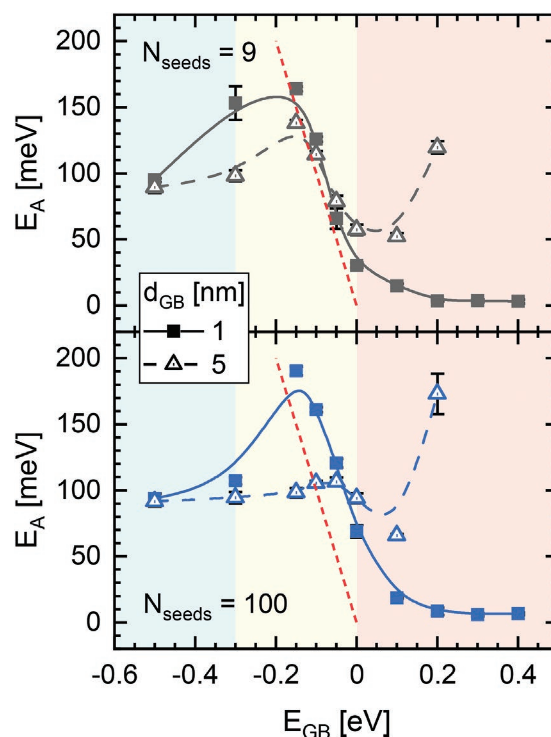

Figure 6. Activation energies from Arrhenius fits to the data in Figure 5 as a function of the GB energy for different GB width as indicated by the line style and symbols alongside with fitting uncertainties. The top graph is for large crystallites, the bottom one for small ones. The background color indicates the different charge transport regimes as explained in the text. Lines are guides to the eye. The red dashed line indicates $E_A = E_{GB}$.

© 2021 The Authors. Advanced Optical Materials published by Wiley-VCH GmbH

quickly fully blocked for thicker boundaries. This evolution is portrait in Figure 6. Furthermore, Figure 6 illustrates the maximum in the activation energy at E_{GB} = –0.15 eV, and the asymptotic approach to a value of (92 ± 2) meV for E_{GB} = –0.5 eV. This value is reached earlier for the wider GB.

Before analyzing and discussing these data in detail, it is instructive to consider how the activation energies evolve for different width and fractions of GB when there is no energy offset between the DOS centers of the crystallites and the GB (**Figure 7**), so that transport is only perturbed by the different degrees of disorder in the two phases, σ_{cryst} = 10 meV and σ_{GB} = 50 meV, respectively. This could, for example, mimic an experimental system in which the GB are simply displaced moieties of the same kind except for additional disorder. We find the mobility follows an Arrhenius law with a deviation at higher temperatures. The two limiting cases are an activation energy of 108 meV when the film consists only out of a single GB, that is, an amorphous film with σ = 50 meV, and a value of (15 ± 5) meV for a single crystal, that is, a value comparable to the DOS width of the crystal. When the film is more polycrystalline yet without GB, the absolute value of the mobility reduces due to the reduced jump rate between crystallites (with $\nu_0 = 10^{13}$ s^{-1}) as compared to the jump rate within the crystallites (with $\nu_0 = 10^{15}$ s^{-1}). Between these two limits, the activation energy increases with the fraction of GB (see also **Table 1** below).

4. Discussion

The aim of our investigation is to explore how (and why) the energy, width, and relative fraction of GB impact on the charge-carrier mobility in a field-effect transistor, with a view to derive guidelines for the film fabrication process. For this,

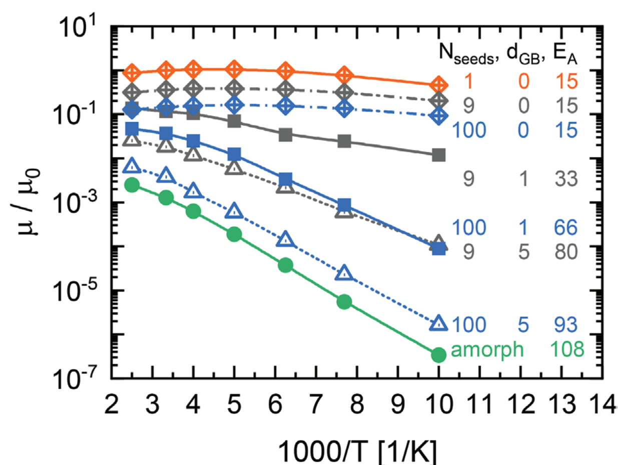

Figure 7. Temperature dependence of the charge-carrier mobility for morphologies with different fractions of crystalline phase with E_{GB} = 0 eV. The number of seeds N_{seeds}, the GB width d_{GB} in nm and the activation energy E_A in meV are indicated next to the corresponding lines. In detail, the orange line corresponds to a single crystal morphology, the green one to the completely amorphous case, black lines and symbols correspond to N_{seeds} = 9, and blue ones to N_{seeds} = 100. The GB width is indicated by the symbol type: crossed diamonds have d_{GB} = 0 nm, filled squares have d_{GB} = 1 nm and dotted triangles have d_{GB} = 5 nm. Lines are guides to the eye.

Table 1. Fraction of GB, Fermi energies, and observed activation energies for the different morphologies.

N_{seeds}	d_{GB} [nm]	fraction of GB [%]	GB site occupancy [%][a)]	$\frac{E_{GB}-E_F}{\sigma}$ [b)]	$E_{GB}-E_F$ [meV]	E_A [meV][c)]
9	1	5	20.0	–0.8	40	33
	3	14	8.0	–1.4	71	–
	5	24	4.6	–1.6	83	66
49	1	11	10.0	–1.3	65	–
	3	31	3.5	–1.8	90	–
	5	49	2.3	–2.0	100	–
100	1	15	7.3	–1.4	70	80
	3	42	2.6	–2.0	100	–
	5	64	1.7	–2.1	105	93
single crystal phase, 1.1% occupancy				–2.0	20	15
single amorphous phase, 1.1% occupancy				–2.3	115	108

a) under the premise that 1.1% charges are localized in the monolayer, and essentially all of them localize in the GB; b) for σ = 50 meV; c) obtained by kMC simulation for E_{GB} = 0, cf. Figure 6.

it is helpful to consider where the charges localize spatially in the transistor, and which occupancy of the DOS results from it. **Figure 8** shows the charge-carrier concentration in the first semiconductor layer for the case of N_{seeds} = 9 (100) seeds and a GB width of d_{GB} = 1 nm (d_{GB} = 5 nm) when a field is applied as indicated by the arrow in the figure. We consider the occupancy with charges when the center of the GB energies ranges from –0.5 eV below the crystallite DOS center to 0.1 eV above. The concentrations for other cases (N_{seeds} = 9, d_{GB} = 5 nm; N_{seeds} = 100, and d_{GB} = 1 and 5 nm) are available as Supporting Information. It is evident that for E_{GB} = –0.5 eV (= 20 k_BT at 300 K), essentially all charges localize in the GB, while some charges can also be found on the crystallites for E_{GB} = –0.1 eV (= 4 k_BT at 300 K). As a result of Coulomb repulsion between the charges (considered explicitly in the simulation up to a cut-off radius of 10 nm), they localize in the crystallite center for the larger crystallites obtained with 9 seeds. For smaller crystallites such as obtained with N_{seeds} = 100, this coulomb repulsion is sufficient to essentially prevent an occupation of the crystallites, implying that charges are exclusively localized in trap sites in the GB, even for shallow traps.

As the GB become energetically more shallow, the occupation of the crystallites with charges increases, with a gradient in carrier density that follows the field, until a perpendicular GB impedes further motion. At that boundary, charges accumulate both in and before the GB, depending on whether the GB sites are statistically of a lower or higher energy as the crystallite site. When the GB represents an energetic barrier, the combined action of the applied field and the carriers' coulomb repulsion leads to a scale-like structure, with a charge density peaking toward the barrier and a depleted zone right after the barrier, in field direction. This scale-like structure closely resembles the structure of capacitively charged GB invoked by Choi and coworkers to account for the lower Hall mobility compared to the OFET mobility in polycrystalline OFETs made from rubrene and made from C8-BTBT embedded in C16IDT-

© 2021 The Authors. Advanced Optical Materials published by Wiley-VCH GmbH

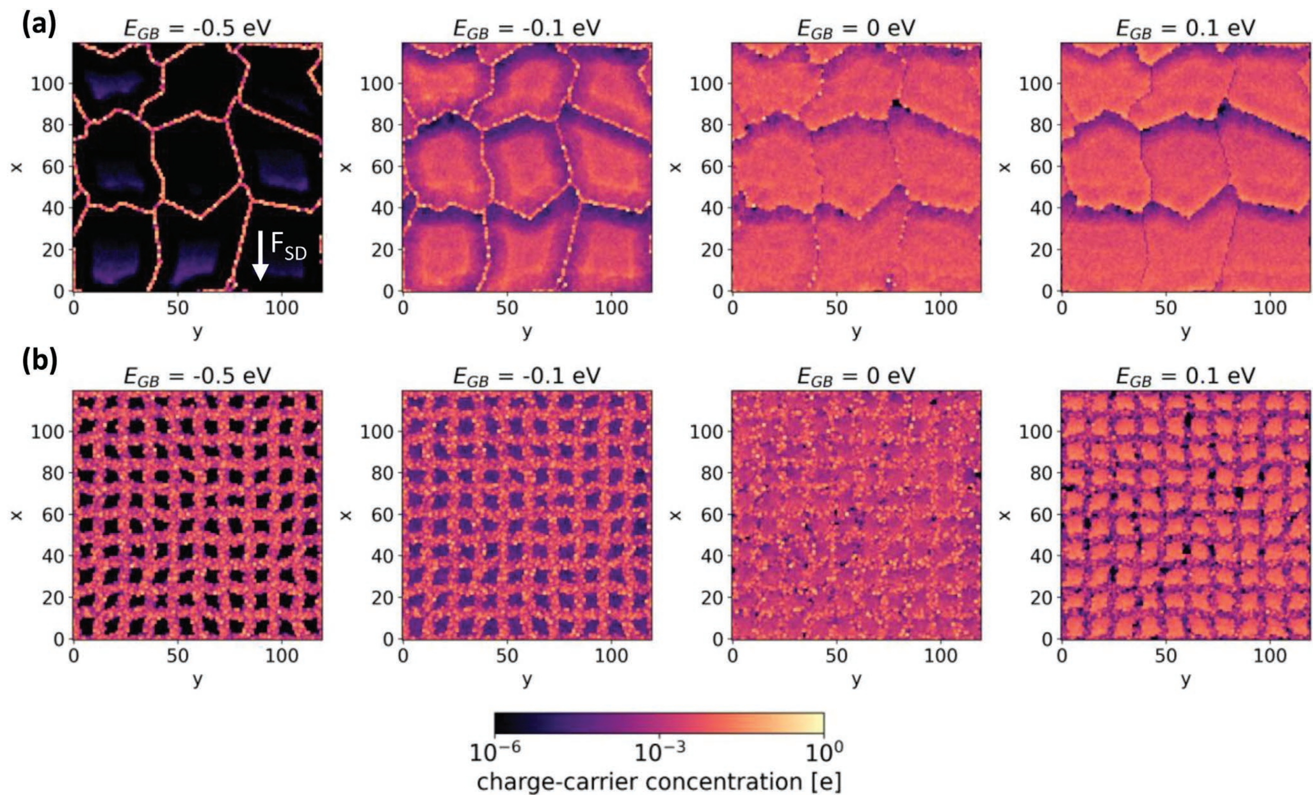

Figure 8. The charge-carrier concentration in the first semiconductor layer for four GB energies at T = 300 K, for the morphology obtained a) with N_{seeds} = 9 and d_{GB} = 1 nm and b) with N_{seeds} = 100 and d_{GB} = 5 nm. The charge-carrier concentration is displayed on a logarithmic color scale, given in units of the elementary charge with orange and yellow colors indicating high concentration. A value of 1 implies a full charge residing at the site for the entire duration of the simulation. The direction of the applied source–drain field is indicated by an arrow. A more complete set can be found in the Supporting Information.

BT.[12a] In summary, we see that depending on the system's parameters, there is a superposition of transport within the GB, transport within the crystallites, and transport between them, all of which occur by different rates.

To assess the impact of GB on charge transport, we next consider the DOS. Under steady state conditions, the charges fill up the DOS distribution so that transport is controlled by thermal activation from the occupied to empty states of the DOS. This mode of transport is fundamentally different from transport within an essentially empty DOS realized, for example, in a time-of-flight experiment in a homogeneous amorphous semiconductor. In the latter case, a charge-carrier jumps from a site distributed around the equilibrium energy $\varepsilon_\infty = -\sigma^2/k_BT$ to a transport energy. Since ε_∞ decreases with temperature, the diffusivity D of charges follows a dependence of $D \propto \exp(-T_0/T)^2$. For σ = 50 meV, at 300 K ε_∞ = −100 meV below the center of the DOS.[26] Here, however, a different transport mode prevails. If all charges were localized homogeneously in one monolayer, the site occupancy for a gate voltage of 5 V would be ≈1%, equivalent to − 2σ below the centre of the DOS. In reality, only about 50–80% of the charges are located in the bottom in-plane layer of the OFET,[15,16] but since the charges are confined to the GB for $E_{GB} \leq 0$, the occupancy in the GB is much greater and well above −2σ. This implies that the GB DOS (which has σ = 50 meV) is filled up at least to the quasi-equilibrium level. Similar considerations can be made for transport within the crystallites. As a consequence, charge transport is controlled by hopping from the Fermi level and should follow a $D \propto \exp(-E_A/k_BT)$ dependence. We have read out the DOS as well as the site occupancies obtained from our simulation for different morphologies and used this to calculate the Fermi level. The values are given in Table 1, along with those obtained for a purely amorphous film (σ = 50 meV) and a single crystal (σ = 10 meV). This is illustrated for a few selected values in **Figure 9**, with the blurred border illustrating the thermal broadening of the Fermi level.

Under this premise, we can analyze the simulated charge-carrier mobilities parametric on the system parameters and temperature. Consider the transport for E_{GB} = 0, where the temperature-dependent simulations presented in Figure 7 indicate a nearly Arrhenius-like temperature dependence for the mobility, and where we could derive the activation energies. As already argued, and evident from Table 1, a Fermi level is established, implying that charges are thermally activated from the Fermi level to a transport level. This thermal activation is well known to result in a Arrhenius-law for the transport of charges. We attribute the deviation obtained at higher temperatures to the fact that the diffusivity D is related to the mobility μ by the Einstein relation $\mu = eD/k_BT$, so that a strictly Arrhenius-type diffusivity translates into a small bend of the mobility values at higher

© 2021 The Authors. Advanced Optical Materials published by Wiley-VCH GmbH

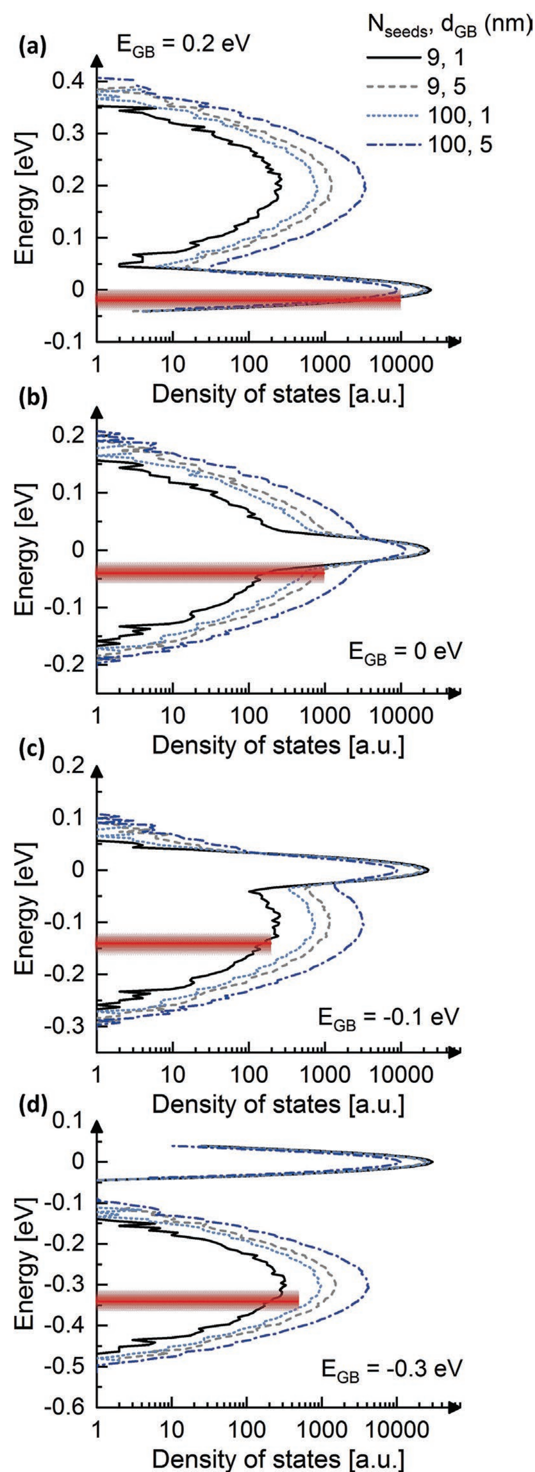

Figure 9. The DOS obtained directly from the simulation for different E_{GB}, a) 0.2 eV, b) 0 eV, c) −0.1 eV, d) −0.3 eV. Different lines indicate morphologies obtained from 9 or 100 seeds, and with a GB width of 1 or 5 nm. The approximate Fermi level for $N_{seeds} = 9$ and $d_{GB} = 1$ nm is indicated by a red bar.

temperatures in an Arrhenius plot. The observed activation energies closely match the Fermi energies. This suggests that the transport level is close to the center of the GB DOS, or, in case of the single crystal, the crystal DOS. The impact of this Fermi-level filling is evident in Figure 7. When changing the morphology from a single crystal to a polycrystalline one with no explicit GB width, just with a change in crystal orientation and a concomitant change in transfer integral (mimicked here by a drop in hopping rate prefactor by 100), we obtain a reduction in the mobility by up to one order of magnitude. The exact value in real systems will depend on how much the transfer integral changes, as demonstrated, for example, by Rivnay and coworkers for perylene-diimide derivatives.[12d] However, inserting even iso-energetic GB of finite width can lower the mobility by a further 1–2 orders of magnitude because transport is trap-limited and the mobility is then controlled by the release of carriers from the Fermi level in the GB.

For GB that are not iso-energetic, we distinguish three regimes.

(i). $E_{GB} < -0.30$ eV ("deep GB"): Thermal activation onto crystallite sites is practically impossible for a separation of more than 10 k_BT at 300 K between GB DOS and crystallite DOS. Transport takes place only within the GB. This is not only confirmed in Figures 8 and 9, but also manifested in the constant value of the activation energy near 80–90 meV that is approached asymptotically for deep GB (Figure 6). It is characteristic for transport in an amorphous phase with corresponding site occupation and resulting Fermi-energy (c.f. Table 1). Transport therefore becomes independent of the actual GB depth. We note that E_{GB} might still impact on injection or extraction in real OFETs, which is not captured in our simulation. As evident from Table 1, the Fermi level will be between 1σ and 2σ below the DOS center of the GB, implying that transport is controlled by the disorder of the GB. For example, reducing σ from 50 to 10 meV increases the mobility by one order of magnitude (see Figure S5, Supporting Information). When transport occurs only in the GB, the dimensionality of the transport path is important. One might expect that the mobility decreases with the width of the GB because the occupancy with charge carriers, and thus the Fermi level, decreases. We find, however, that μ increases by roughly a factor of 20 when d_{GB} increases from 1 to 3 nm (Figure 4) and further by a factor of 2 when d_{GB} reaches 5 nm. The reason is that when $d_{GB} = 1$ nm, the GB form a 1D network. Considering an occupancy of roughly 20%, coulomb blockade limits the mobility severely. The blockade is progressively suspended as d_{GB} increases. The insight gained from this is clear. If you cannot avoid GB with a mean energy well below your crystallite sites, they should at least be reasonably wide, well ordered, and better more of them than less. In passing we note that such a situation can also arise in the binary acceptor phase of ternary blends used for organic solar cells.[30,31] The practically more relevant case is likely to be the regime where some transport also proceeds via the crystallites.

(ii). -0.30 eV $< E_{GB} < 0$ eV ("shallow GB"): The highest mobility, and concomitantly lowest activation energy is obtained for iso-energetic GB. As the center energy of the GB reduces, the activation energy increases linearly. As evident from Figure 6 for -0.15 eV $< E_{GB} < 0$ eV, we phenomenologically find $E_A = -E_{GB} + (E_{GB} - E_F)$, that is, the Fermi level offset from the center of the GB DOS, and the absolute value of the GB center together give the resulting activation energy. Obviously, the

© 2021 The Authors. Advanced Optical Materials published by Wiley-VCH GmbH

charge-carriers are localized in the GB and have to be activated to the transport level near the center of the crystallite DOS, that is, spatially onto the crystallites. This linear increase in E_A translates directly into an exponential decrease of the carrier mobility, as evidenced in Figure 4. The increase in E_A with decreasing E_{GB} continues up to about $E_{GB} = -150$ meV, beyond which E_A decreases. It seems that this maximum in E_A, which corresponds to the point of inflection of the $\mu(E_{GB})$-curve (Figure 4), indicates the energy that divides trap-limited transport across the crystallites from a transport predominantly in the GB. From this analysis, we find that the design guidelines for shallow GB are opposite to those of deep GB. For shallow GB, high mobilities require a Fermi level close to the center of the GB DOS. This is best realized when GB are narrow and few (c.f. Figure 4 and Table 1). The increase of OFET mobility with the reduction in GB is well documented, for example, for perylene-diimide based OFETs.[7a] A low disorder will, of course, still be beneficial, and it is trivial to mention that the GB should be as shallow as possible.

(iii). 0 eV < E_{GB} ("energetic barriers"): When the GB energy becomes positive, the GB act as barriers for charge transport, and μ decreases exponentially as the activation energy required to overcome the barrier increases. One would expect an activation energy that is composed of the absolute value of the Fermi energy and the height of the GB center (see Figure 9), that is, $E_A = E_{GB} + (E_{cryst} - E_F)$. We recall that when the GB form a barrier, the Fermi level is ≈20 meV below the center of the crystal DOS, which is at 0 eV. However, from Figure 6 we observe that the activation energy is ≈30–40 meV lower that the expected value. This suggests that the transport occurs preferentially through the tail states of the GB DOS.

For thin GB, $d_{GB} = 1$ nm, the constant mobility value when E_{GB} exceeds 0.15 eV indicates that tunneling through the barrier between the crystallites occurs and becomes the rate limiting process. In principle, a low level of tunneling will also take place for thicker barriers, yet this process is not captured for the parameters used in our simulation.

In summary, our study demonstrates how GB can reduce the theoretically possible mobility of a single crystal, or even a polycrystalline film by several orders of magnitude. Key parameters are the energy of the GB, their disorder and their width, which impacts on the dimensionality of charge transport as well as on their Fermi level. Changes to the mobility resulting from varying the Fermi level through modifications of the gate voltage (or channel length) have not been considered here to keep the study reasonably concise. To a first approximation, we expect a higher Fermi level associated with higher gate voltages to increase the overall mobility and to shift the boundary for distinction between deep and shallow GB to lower energies. Coulomb repulsion of carriers trapped in the GB was found to repel mobile carriers from the GB toward the crystallite centers. While evident when plotting the charge-carrier concentration (Figure 8), we did not notice a particular influence of these coulomb wells (followed by the GB troughs) on the overall mobility, which seemed to be dominated by the energetics of the GB and Fermi level. Based on the earlier work by Bobbert and coworkers, we expect however an impact of the Coulomb repulsion on the vertical distribution of charges.[15]

5. Conclusions

We have presented a study on the impact of GB on charge transport in OFETs. The morphologies we created mimic a molecular film rather than a polymeric one, where tie chains would play a critical role.[32]

For energetically deep GB, we find that transport is filamentary and occurs predominantly in the boundaries, so that it is facilitated by a reasonably dense network of wide boundaries with a low degree of disorder. As GB become shallower, transport occurs predominantly on the crystallites yet is limited by trapping and thermal detrapping from the Fermi level in the GB. This detrapping process is alleviated for narrow and well-ordered boundaries where the Fermi level is higher. When the GB are energetic barriers, they need to be overcome by tunneling, when the barrier is thin enough, or thermal activation over the barrier. Both severely reduce the charge-carrier mobility.

Our study demonstrates the important role of the Fermi level in controlling the OFET mobility for the probably most frequently encountered case of shallow traps. Notably, the reduction in mobility compared to a single crystal value can be kept limited for narrow, ordered and energetically shallow GB. In many simulations, the site occupancy and the formation of the Fermi level is frequently neglected, even though this controls the temperature dependence and absolute value of the mobility. We hope that our work might stimulate a more explicit consideration of the Fermi level in future simulations with perhaps more sophisticated morphologies.

Supporting Information

Supporting Information is available from the Wiley Online Library or from the author.

Acknowledgements

T.M. would like to thank Rishabh Saxena for valuable discussions on simulation techniques. The authors are grateful to the Simbeyond support team, and in particular to Stefano Gottardi, for constructive advice. This work was supported by Bayrisches Staatsministerium für Wissenschaft und Kunst through the Initiative Solar Technologies go Hybrid.

Open access funding enabled and organized by Projekt DEAL.

Conflict of Interest

The authors declare no conflict of interest.

Data Availability Statement

The data that support the findings of this study are available from the corresponding author upon reasonable request.

© 2021 The Authors. Advanced Optical Materials published by Wiley-VCH GmbH

Keywords

activation energy, charge mobility, Monte-Carlo simulations, morphology, organic field-effect transistors, organic semiconductor

Received: January 19, 2021
Revised: March 17, 2021
Published online: May 7, 2021

[1] a) W. Helfrich, W. G. Schneider, *Phys. Rev. Lett.* **1965**, *14*, 229; b) A. Sano, M. Pope, H. Kallmann, *J. Chem. Phys.* **1965**, *43*, 3367.
[2] H. Kleemann, K. Krechan, A. Fischer, K. Leo, *Adv. Funct. Mater.* **2020**, *30*, 1907113.
[3] a) J. H. Burroughes, C. A. Jones, R. H. Friend, *Nature* **1988**, *335*, 137; b) G. Horowitz, D. Fichou, X. Peng, Z. Xu, F. Garnier, *Solid State Commun.* **1989**, *72*, 381.
[4] a) J.-I. Park, J. W. Chung, J.-Y. Kim, J. Lee, J. Y. Jung, B. Koo, B.-L. Lee, S. W. Lee, Y. W. Jin, S. Y. Lee, *J. Am. Chem. Soc.* **2015**, *137*, 12175; b) N. Kurihara, A. Yao, M. Sunagawa, Y. Ikeda, K. Terai, H. Kondo, M. Saito, H. Ikeda, H. Nakamura, *Jpn. J. Appl. Phys.* **2013**, *52*, 05DC11.
[5] a) V. Coropceanu, J. Cornil, D. A. da Silva Filho, Y. Olivier, R. Silbey, J.-L. Brédas, *Chem. Rev.* **2007**, *107*, 926; b) H. Bässler, A. Köhler, in *Unimolecular and Supramolecular Electronics I*, Vol. *312* (Ed: R. M. Metzger), Springer, Berlin **2011**, Ch. 1; c) H. Sirringhaus, T. Sakanoue, J.-F. Chang, *Phys. Status Solidi B* **2012**, *249*, 1655; d) S. Fratini, D. Mayou, S. Ciuchi, *Adv. Funct. Mater.* **2016**, *26*, 2292; e) S. Fratini, M. Nikolka, A. Salleo, G. Schweicher, H. Sirringhaus, *Nat. Mater.* **2020**, *19*, 491.
[6] a) D. Venkateshvaran, M. Nikolka, A. Sadhanala, V. Lemaur, M. Zelazny, M. Kepa, M. Hurhangee, A. J. Kronemeijer, V. Pecunia, I. Nasrallah, I. Romanov, K. Broch, I. McCulloch, D. Emin, Y. Olivier, J. Cornil, D. Beljonne, H. Sirringhaus, *Nature* **2014**, *515*, 384; b) K. Takimiya, S. Shinamura, I. Osaka, E. Miyazaki, *Adv. Mater.* **2011**, *23*, 4347; c) G. Schweicher, G. Garbay, R. Jouclas, F. Vibert, F. Devaux, Y. H. Geerts, *Adv. Mater.* **2020**, *32*, 1905909.
[7] a) I. Vladimirov, M. Kellermeier, T. Geßner, Z. Molla, S. Grigorian, U. Pietsch, L. S. Schaffroth, M. Kühn, F. May, R. T. Weitz, *Nano Lett.* **2018**, *18*, 9; b) K. Zhang, Z. Wang, T. Marszalek, M. Borkowski, G. Fytas, P. W. M. Blom, W. Pisula, *Mater. Horiz.* **2020**, *7*, 1631.
[8] M. Kim, S. U. Ryu, S. A. Park, K. Choi, T. Kim, D. Chung, T. Park, *Adv. Funct. Mater.* **2020**, *30*, 1904545.
[9] H. F. Haneef, A. M. Zeidell, O. D. Jurchescu, *J. Mater. Chem. C* **2020**, *8*, 759.
[10] a) F. Steiner, C. Poelking, D. Niedzialek, D. Andrienko, J. Nelson, *Phys. Chem. Chem. Phys.* **2017**, *19*, 10854; b) I. Vladimirov, M. Kühn, T. Geßner, F. May, R. T. Weitz, *Sci. Rep.* **2018**, *8*, 14868.
[11] G. Horowitz, M. E. Hajlaoui, R. Hajlaoui, *J. Appl. Phys.* **2000**, *87*, 4456.
[12] a) H. H. Choi, A. F. Paterson, M. A. Fusella, J. Panidi, O. Solomeshch, N. Tessler, M. Heeney, K. Cho, T. D. Anthopoulos, B. P. Rand, V. Podzorov, *Adv. Funct. Mater.* **2020**, *30*, 1903617; b) J. Chen, C. K. Tee, M. Shtein, J. Anthony, D. C. Martin, *J. Appl. Phys.* **2008**, *103*, 114513; c) X. Li, A. Kadashchuk, I. I. Fishchuk, W. T. T. Smaal, G. Gelinck, D. J. Broer, J. Genoe, P. Heremans, H. Bässler, *Phys. Rev. Lett.* **2012**, *108*, 066601; d) J. Rivnay, L. H. Jimison, J. E. Northrup, M. F. Toney, R. Noriega, S. Lu, T. J. Marks, A. Facchetti, A. Salleo, *Nat. Mater.* **2009**, *8*, 952; e) H. T. Nicolai, M. Kuik, G. A. H. Wetzelaer, B. Boer, C. Campbell, C. Risko, J. L. Brédas, P. W. M. Blom, *Nat. Mater.* **2012**, *11*, 882.
[13] R. A. Street, J. E. Northrup, A. Salleo, *Phys. Rev. B* **2005**, *71*, 165202.
[14] O. Simonetti, L. Giraudet, *Polym. Int.* **2019**, *68*, 620.
[15] A. Sharma, F. W. A. van Oost, M. Kemerink, P. A. Bobbert, *Phys. Rev. B* **2012**, *85*, 235302.
[16] H. Li, Y. Li, H. Li, J.-L. Brédas, *Adv. Funct. Mater.* **2017**, *27*, 1605715.
[17] a) W. L. Kalb, S. Haas, C. Krellner, T. Mathis, B. Batlogg, *Phys. Rev. B* **2010**, *81*, 155315; b) G. Horowitz, M. E. Hajlaoui, *Adv. Mater.* **2000**, *12*, 1046; c) A. Di Carlo, F. Piacenza, A. Bolognesi, B. Stadlober, H. Maresch, *Appl. Phys. Lett.* **2005**, *86*, 263501; d) A. B. Chwang, C. D. Frisbie, *J. Appl. Phys.* **2001**, *90*, 1342.
[18] S. Verlaak, P. Heremans, *Phys. Rev. B* **2007**, *75*, 115127.
[19] a) K. Puntambekar, J. Dong, G. Haugstad, C. D. Frisbie, *Adv. Funct. Mater.* **2006**, *16*, 879; b) M. Tello, M. Chiesa, C. M. Duffy, H. Sirringhaus, *Adv. Funct. Mater.* **2008**, *18*, 3907; c) L. C. Teague, B. H. Hamadani, O. D. Jurchescu, S. Subramanian, J. E. Anthony, T. N. Jackson, C. A. Richter, D. J. Gundlach, J. G. Kushmerick, *Adv. Mater.* **2008**, *20*, 4513; d) C. Qian, J. Sun, L. Zhang, H. Huang, J. Yang, Y. Gao, *J. Phys. Chem. C* **2015**, *119*, 14965.
[20] M. J. Jaquith, J. E. Anthony, J. A. Marohn, *J. Mater. Chem.* **2009**, *19*, 6116.
[21] M. Mladenović, N. Vukmirović, I. Stanković, *J. Phys. Chem. C* **2013**, *117*, 15741.
[22] T. W. Kelley, C. D. Frisbie, *J. Phys. Chem. B* **2001**, *105*, 4538.
[23] a) S. Verlaak, V. Arkhipov, P. Heremans, *Appl. Phys. Lett.* **2003**, *82*, 745; b) G. Horowitz, *Adv. Funct. Mater.* **2003**, *13*, 53.
[24] a) M. adenović, N. Vukmirović, *J. Phys. Chem. C* **2015**, *119*, 23329; b) L. G. Kaake, P. F. Barbara, X.-Y. Zhu, *J. Phys. Chem. Lett.* **2010**, *1*, 628.
[25] A. Miller, E. Abrahams, *Phys. Rev.* **1960**, *120*, 745.
[26] H. Bässler, *Phys. Status Solidi B* **1993**, *175*, 15.
[27] J. J. M. van der Holst, F. W. A. van Oost, R. Coehoorn, P. A. Bobbert, *Phys. Rev. B* **2011**, *83*, 482.
[28] M. S. Tamboli, P. K. Palei, S. S. Patil, M. V. Kulkarni, N. N. Maldar, B. B. Kale, *Dalton Trans.* **2014**, *43*, 13232.
[29] S. R. Mohan, M. P. Singh, M. P. Joshi, *J. Polym. Sci., Part B: Polym. Phys.* **2019**, *57*, 137.
[30] M.-A. Pan, T.-K. Lau, Y. Tang, Y.-C. Wu, T. Liu, K. Li, M.-C. Chen, X. Lu, W. Ma, C. Zhan, *J. Mater. Chem. A* **2019**, *7*, 20713.
[31] N. Gasparini, A. Salleo, I. McCulloch, D. Baran, *Nat. Rev. Mater.* **2019**, *4*, 229.
[32] F. Segatta, G. Lattanzi, P. Faccioli, *Macromolecules* **2018**, *51*, 9060.

© 2021 The Authors. Advanced Optical Materials published by Wiley-VCH GmbH